RSC Advances

PAPER

View Article Online
View Journal | View Issue

Cite this: *RSC Adv.*, 2025, **15**, 12364

Mechanistic study on the photocatalytic degradation of rhodamine B *via* Mn–Schiff-base-modified Keggin-type polyoxometalate composite materials†

Chang Man,[a] Chunpeng Xu,[b] Jinfeng Wang,[b] Xiangli Li,[b] Tong Li,[b] Yanhua Ma,[b] Shalu Zhang,[b] Yongfeng Qiao*[bc] and Qiong Wu *[bc]

Organic–inorganic hybrid materials have significant potential in the photocatalytic degradation of Rhodamine B (RhB). In this study, five hybrid materials were successfully synthesized by modifying silicotungstic acid ($H_4SiW_{12}O_{40}$, abbreviated $SiW_{12}O_{40}$) with diverse MnL [L = Salen(L^1), 5-Br-Salen(L^2), 5-Cl-Salen(L^3), 3-Me-Salen(L^4), di-*t*Bu-Salen(L^5)] complexes, specifically derivatives featuring various substituents. All the compounds are characterized by IR spectra, elemental analyses and thermogravimetric analyses (TGA). The band gaps of 1.33–1.52 eV and energy bands are obtained through the measurement of UV-Vis DRS and Mott–Schottky. Photocatalytic experiments of $(MnL^1)_4SiW_{12}O_{40}$ (compound **1**), $(MnL^2)_4SiW_{12}O_{40}$ (compound **2**), $(MnL^3)_4SiW_{12}O_{40}$ (compound **3**), $(MnL^4)_4SiW_{12}O_{40}$ (compound **4**) and $(MnL^5)_4SiW_{12}O_{40}$ (compound **5**) indicate that compound **2** catalyst exhibits the best photocatalytic properties (RhB degrades to 6% during 70 min) while all of them possess catalytic activity for photodegradation of RhB under UV irradiation. Free radical trapping experiments show that the addition of PBQ ($\cdot O_2^-$ trapping agents) makes the RhB residual ratio increase from 6% to 60% and indicates that $\cdot O_2^-$ is playing a pivotal role. A possible mechanism of RhB photodegradation in the presence of compound **2** is proposed based on free radical trapping experiments and the energy bands. Future work could focus on fine-tuning the molecular architecture through strategic modification of the organic ligands and precise control of the metal-to-POM ratio, potentially leading to optimized electronic structures and enhanced charge transfer kinetics for superior photocatalytic performance in environmental applications.

Received 27th November 2024
Accepted 20th March 2025

DOI: 10.1039/d4ra08382b

rsc.li/rsc-advances

1 Introduction

Semiconductor photocatalysis has attracted increasing attention for its potential applications in environmental and energy-related fields, including organic pollutant degradation[1] and hydrogen production.[2] Compared with traditional treatment methods, this technology can directly convert solar energy into chemical energy, thereby reducing secondary pollution. However, early studies largely centered on titanium dioxide (TiO_2) and zinc oxide (ZnO). While these are inexpensive and widely available,[3,4] their wide band gaps limit their ability to absorb visible light, resulting in low photocatalytic efficiency. Developing novel semiconductors responsive to visible light has thus become a key approach for improving photocatalytic performance.

Polyoxometalates (POMs) are a class of metal–oxygen anionic clusters with clear molecular structures, strong tunability, and excellent redox properties, making them highly promising in catalysis. Incorporating heteropoly acids into conventional semiconductors can yield composite catalysts with enhanced visible-light responsiveness.[5,6] Previous studies have shown that POM-based composite materials, prepared through immobilization and other assembly strategies, can significantly boost photocatalytic activity under visible-light irradiation. For instance, Anandan and Yoon synthesized a nanoporous phosphotungstic-acid–TiSB-15 material modified with photosensitive molecules, achieving a considerable improvement in the degradation efficiency of methyl orange.[7] Despite such progress, effectively enhancing sunlight absorption while leveraging the intrinsic characteristics of POMs remains challenging.

Further work by Qiong Wu involved combining A/B-type Anderson heteropolyanions with Mn(III)–Schiff-base

[a]School of Physical Science and Technology, Kunming University, No. 2 Pu Xin Road, Economic and Technological Development Zone, Kunming, Yunnan Province, 650214, China

[b]School of Chemistry and Chemical Engineering, Kunming University, No. 2 Pu Xin Road, Economic and Technological Development Zone, Kunming, Yunnan Province, 650214, China

[c]Yunnan Key Laboratory of Metal-Organic Molecular Materials and Device, School of Chemistry and Chemical Engineering, Kunming University, China. E-mail: qiaoyongfengkum@163.com; wuqiongkm@163.com

† Electronic supplementary information (ESI) available. See DOI: https://doi.org/10.1039/d4ra08382b

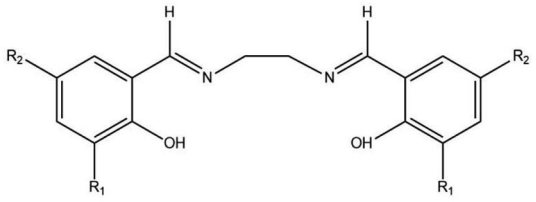

L^1: R_1,R_2=H; L^2: R_1=H, R_2=Br; L^3: R_1=H, R_2=Cl;
L^4: R_1=CH_3, R_2=H ; L^5: R_1, R_2=tBu

Scheme 1 Schematic representation of L (L = L^1, L^2, L^3, L^4, L^5).

coordination complexes, demonstrating photocatalytic degradation capabilities.[8,9] In parallel, Meng and colleagues designed metal–Salens along with Keggin-type clusters, constructing four photocatalytic materials effective in degrading RhB.[10] Computational studies by Zhongmin Su's group revealed that POM moieties function as electron acceptors, while organic fragments act as electron donors, thereby fine-tuning the molecular energy-level gap and facilitating efficient charge transfer in hybrid systems.[11–13]

Nevertheless, most existing research has focused on specific ligands or certain types of POM, and systematic efforts to modulate the electronic effects of ligands to adjust band gaps and enhance visible-light responsiveness are relatively limited. To address this gap, the present study introduces five ligands (L = Salen(L^1), 5-Br-Salen(L^2), 5-Cl-Salen(L^3), 3-Me-Salen(L^4), di-*t*Bu-Salen(L^5)), each with distinct electronic effects, and combines them with a Keggin-type POM ($H_4SiW_{12}O_{40}$, hereafter referred to as $SiW_{12}O_{40}$) to synthesize a series of POM–Mn–Schiff-base hybrid materials (see Scheme 1). By employing UV-Vis DRS and Mott–Schottky measurements, we systematically examine the conduction and valence bands and band-gap widths of these materials. We also investigate their photocatalytic degradation of RhB and propose a possible mechanism based on our findings. This work offers fresh insights into the rational design and performance enhancement of POM-based photocatalytic materials.

2 Experimentation

2.1 Materials

MnL (L = L^1, L^2, L^3, L^4, L^5) was synthesized by aldehydes salicylaldehyde, ethylenediamine and manganese perchlorate as precursors. These precursors were then mixed with silicotungstic acid ($H_4SiW_{12}O_{40}$, abbreviated $SiW_{12}O_{40}$) to form $(MnL)_4SiW_{12}O_{40}$ (L = L^1, L^2, L^3, L^4, L^5). Ethylenediamine, salicylaldehyde, 5-bromosalicylaldehyde, 5-chlorosalicylaldehyde, trimethylsalicylaldehyde and 3,5-di-*tert*-butylsalicylaldehyde were purchased from Aladdin, manganese perchlorate was obtained from Tianjin Windship Chemical reagent, and $SiW_{12}O_{40}$ was procured from Rohen's reagent. None of the chemicals listed above were applied directly without first undergoing purification.

2.2 Preparation of photocatalytic material $(MnL)_4SiW_{12}O_{40}$ (L = L^1, L^2, L^3, L^4, L^5)

Salicylaldehyde (0.244 g, 2 mmol) was dissolved in 15 mL of methanol to form solution A, while ethylenediamine (0.060 g, 1 mmol) was dissolved in a separate 15 mL methanol solution to form solution B. Solution B was then transferred to solution A, and the mixture was stirred at room temperature using a constant-temperature magnetic stirrer for 2 h to yield a significant amount of yellow solid, with subsequent addition of ethanol (15 mL) of $Mn(ClO_4)_2\cdot 6H_2O$ (0.362 g, 1 mmol). A deep-brown solution was obtained, which was refluxed for 2 h, then allowed to stand at room temperature. The resulting solution was mixed and stirred well, and then 2 mL (0.040 g, 1 mmol) of aqueous sodium hydroxide solution was added. It was refluxed with stirring for 2 h, and then left to stand at room temperature to obtain a large number of dark brown massive crystals, which were filtered to leave the filter residue to obtain MnL^1, as reported in ref. 14. $SiW_{12}O_{40}$ (2.878 g, 0.1 mmol) was dissolved in 20 mL distilled water. Then, 20 mL MnL^1 (0.128 g, 0.4 mmol) methanol solution was quickly added. It was placed in a constant temperature magnetic stirrer and stirred at a constant temperature of about 40 °C for 5 min after which a large amount of brownish reaction mixture appeared. The tan mixture was stirred at 35 °C for two days and the precipitate was obtained by filtration. The precipitate was recrystallised in 20 mL of mixed solution (CH_2Cl_2 : CH_3OH = 1 : 1). The crystal $(MnL^1)_4SiW_{12}O_{40}$ (compound **1**) was obtained in about one week.[15] Replacement of salicylaldehyde with 2 mmol of 5-bromosalicylaldehyde (0.402 g), 5-chlorosalicylaldehyde (0.313 g), 3-methylsalicylaldehyde (0.272 g), and 3,5-di-*tert*-butylsalicylaldehyde (0.468 g), respectively, gave $(MnL^2)_4SiW_{12}O_{40}$ (compound **2**), $(MnL^3)_4SiW_{12}O_{40}$ (compound **3**), $(MnL^4)_4SiW_{12}O_{40}$ (compound **4**) and $(MnL^5)_4SiW_{12}O_{40}$ (compound **5**).

2.3 Characterizations

A Fourier transform infrared spectrometer (VERTEX-70) was used to collect the infrared spectra of the samples that were recorded. To assess thermal stability, thermogravimetric analysis was conducted on a METTLER TOLEDO TGA/DSC^{3+} instrument under nitrogen atmosphere, with a temperature range of 30 °C to 1000 °C, and a heating rate of 10 °C min^{-1}. Solid-state UV diffuse reflectance spectroscopy is a widely employed technique for assessing the light absorption characteristics of semiconductor materials.[16–18] Reflectance spectra of the catalysts were measured between 200 and 800 nm using a Shimadzu UV-2450 UV-visible spectrophotometer in order to determine its forbidden bandwidth. An electrochemical workstation (Autolap, Aptar China Co., Ltd, Switzerland) was employed for Mott–Schottky plots, electrochemical impedance spectra (EIS), and the transient photocurrent. The standard three-electrode system was composed of the photocatalyst (20 mg sample impregnated with two drops of α-glycerol loaded on a 2.0 cm^2 ITO glass which was cleaned with ethanol ultrasound), a platinum sheet, and a calomel electrode(saturated KCl solution), which were used as the working electrode, counter electrode, and reference electrode in the test system. The transient photocurrent test of the sample was carried out in 0.1 M Na_2SO_4 aqueous solution with a 300 W xenon lamp. The electrochemical impedance spectroscopy test of the sample was carried out in 0.1 M potassium ferricyanide solution.

2.4 Photocatalytic activity identification

Rhodamine B (RhB) was used to simulate pollutants in water by taking 100 mL of RhB (10 mg L^{-1}) and adjusting the solution pH to 3.5 with HCl and NaOH. Following a 30-minute dark treatment, 50 mg of $(MnL)_4SiW_{12}O_{40}$ (L = L^1, L^2, L^3, L^4, L^5) (compounds **1–5**) was introduced to reach the adsorption–desorption equilibrium. The photocatalytic degradation process was conducted under a 400 W xenon lamp (CEL-SPH2N-D5) at a constant temperature of 25 °C, with samples collected every 15 minutes. An electric centrifuge (80-1) facilitated the separation of catalyst and solution, with the supernatant discarded. The photocatalytic activity of compounds **1–5** was assessed by measuring the maximum absorption peak of the RhB solution using a UV spectrophotometer. To validate the catalyst's photocatalytic activity, each separated catalyst underwent three washes with deionized water, dried, and underwent a cycling experiment with identical degradation conditions. Degradation rates were calculated from the Lambert–Beer law:[19]

$$\eta = (C_t/C_0) \times 100\% \quad (1)$$

C_0 is the initial absorbance of RhB when adsorption equilibrium is reached, and C_t is the absorbance of RhB at light time t (in min).

3 Results and discussion

3.1 Fourier-transform infrared spectroscopy

Fig. 1 illustrates the FT-IR spectra of MnL^1 and compounds **1–5** with distinct vibrational bands between 400 and 4000 cm^{-1}. In the spectrum of MnL^1, 1539 cm^{-1} is attributed to the ν (C=C) vibration of aromatic compounds and 1625 cm^{-1} to the ν (C=N) stretching vibration, suggesting that salicylaldehyde and ethylenediamine monomers underwent a Schiff-base reaction to produce C=N, while the integrity of the salicylaldehyde benzene ring was maintained. The absorption peak at 547 cm^{-1} in the fingerprint region is related to the Mn–N vibration, while the absorption peak at 466 cm^{-1} is related to the Mn–O vibration, and these two absorption peaks indicate the occurrence of coordination reaction between Salen and manganese, which provides strong evidence for the successful preparation of MnL^1.[20,21] In compounds **1–5**, the peaks at 796, 926, 980 and 1016 cm^{-1} correspond to the vibrations of the ν (Si–O), ν (W=Ot), ν (W–Ob) and ν (W–Oc) bonds, respectively, which are characteristic of $[SiW_{12}O_{40}]^{4-}$,[22] suggesting that $[SiW_{12}O_{40}]^{4-}$ is present in all of the components of compounds **1–5**. FT-IR analysis reveal the presence of the broad –OH stretching bands around 3400 cm^{-1} showing the presence of possible solvent molecules *e.g.* water and methanol in the compounds **1–5**.[21] However, the above data can not determine the compositional ratio between its building units.

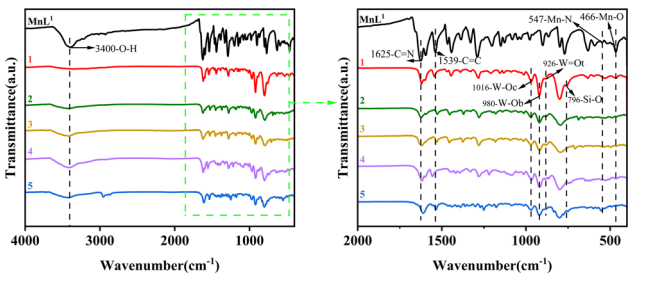

Fig. 1 Fourier transform infrared spectra of MnL^1 and compounds **1–5**.

3.2 Organic and metal elemental analysis

An organic elemental analyser and ICP mass spectrometry (ICP-MS) (hereafter, ICP) were used to solve the mentioned issue in 3.1 section and the results were shown in Table S1.† Compounds **1–5** were synthesized by keeping the molar ratios of MnL to $SiW_{12}O_{40}$ at 4 : 1. For compound **1**, the mass fractions of carbon (C), nitrogen (N), manganese (Mn) and tungsten (W) were measured to be 17.53, 2.59, 5.04 and 50.41, respectively, and the molar ratios of carbon (C), nitrogen (N), manganese (Mn) and tungsten (W) were calculated to be 15.92, 2.02, 1.00 and 2.99. The result indicates that compound **1** was synthesized successfully by keeping the molar ratios of MnL^1 to $SiW_{12}O_{40}$ at 4 : 1. The same conclusion can be obtained by analysing the elemental analysis data of compounds **2–5**.

These elemental analysis results reflect that the atomic number ratio of W and Mn is 3 : 1, which reveal the proportional unit of the five compounds has been constructed. Followed by comparing the data of the solvent-free theoretical values and combining with the FT-IR data, however, it was further surmised that the compounds **1–5** contained solvent molecules.

3.3 Thermogravimetric analysis

To further determine whether compounds **1–5** contained solvents, the thermal stability of MnL^1 and compounds **1–5** were investigated using TGA (Fig. 2) in the range of 30.0–1000.0 °C under nitrogen assistance. The first weight loss of MnL^1 occurred at 70.5–126.0 °C, which was attributed to water and solvent losses, with a weight loss of about 7.58%, and this

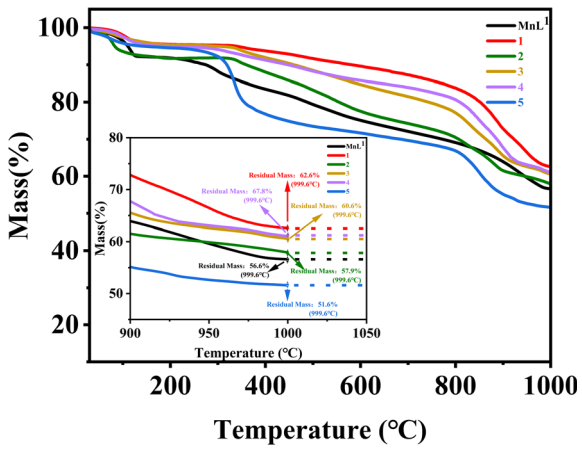

Fig. 2 Thermogravimetric analysis (TGA) curves of MnL^1 and compounds **1–5**.

weight loss has also been documented in the literature.[10] The second (23.79%) and third weight loss (9.04%) occurred at 268.2–860.9 °C and 860.9–977.7 °C, respectively, which may be attributed to the decomposition of the organic ligand, and the final residual amount of the product may be manganese oxide. Compounds **1–5** have similar weight loss trends. There are three weight loss stages. Among them, the first weight loss stage was in the interval of 58.0–217.5 °C, and compounds **1–5** all showed obvious evaporation of solvent moleculars, with a weight loss of 4.63%, 8.19%, 4.66%, 5.14% and 5.25%, respectively. The decomposition of organic ligands and the collapse of the $SiW_{12}O_{40}$ structure occur in the range of 290.0–622.0 °C and 789.0–1000.0 °C.

Based on the above analysis, it is found that the mass fractions of the with-solvent theoretical values are smaller than that of the solvent-free ones. Compound **1**, for example, the mass of 4.63% solvent makes the with-solvent calculated mass fractions (C, N, Mn and W) turn to 17.62, 2.57, 5.04 and 50.58 (Table S1†), respectively which are in close agreement with the experimental values. There will be solvent molecules in the preparation process of photocatalysts, which are related to the composition of the reaction system of the solvent. This phenomenon has been reported in the literature by TGA.[23,24]

3.4 XPS spectra

X-ray photoelectron spectroscopy (XPS) measurement was performed to further identify the chemical composition and valence states of compounds **1–5**. The binding energies were determined using C1s at 284.8 eV as a reference for charge correction. Fig. 3(a) shows the survey spectra of compounds **1–5** confirming the presence of the elements C, N, O, Mn, Si, W, Br, Cl. The corresponding high-resolution XPS spectra of Mn, Si, W of compound **2** are shown in Fig. 3(b–d), respectively. For the high resolution spectra of Mn (Fig. 3(b)), two peaks are observed at 653.47 and 641.95 eV, with a separation of 11.52 eV, which are attributed to Mn $2p_{1/2}$ and Mn $2p_{3/2}$, respectively, indicating the Mn^{3+} oxidation state.[25] Binding energies of Si 2p in the silicotungstate anion were observed at 102.64 and 101.69 eV. Two peaks were observed at 38.13 and 35.93 eV, attributed to W $4f_{5/2}$ and W $4f_{7/2}$, respectively.[26] In summary, the presence of Mn 2p, Si 2p and W 4f signals confirmed the successful formation of compound **2**.

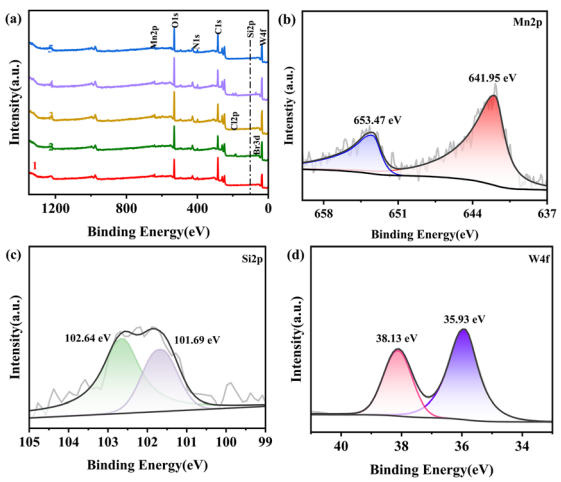

Fig. 3 XPS(a) survey spectra of compounds **1–5**, and high resolution spectra of (b) Mn 2p, (c) Si 2p and (d) W 4f of compound **2**.

3.5 Solid-state UV diffuse reflectance

The UV-visible diffuse reflectance spectroscopy (UV-Vis DRS) data, depicted in Fig. 4(a), captures the material's absorption profile from 200 to 800 nm. Given the observed absorption within this range, it is assumed that these compounds may exhibit photocatalytic degradation under visible light spectrum. The forbidden bandwidth can be calculated using the following equation:

$$A = C(h\nu - E_g)^{(n/2)}/h\nu \quad (2)$$

where A represents the absorption coefficient, ν denotes the optical frequency, E_g denotes the forbidden bandwidth, and C is a constant. The bandgap value, n, varies depending on the properties of semiconductor, with direct semiconductors having $n = 1$ and indirect semiconductors having $n = 4$. Through the solid-state UV diffuse reflection data and the optical gap formula to draw the horizontal coordinate $h\nu$ and vertical coordinate $Ah\nu$ curve, along the curve of the longest part of the straight line to do the tangent, tangent and x-axis intersection that is the width of the forbidden band. As illustrated in Fig. 4(b), the band gaps of the five compounds were 1.56 eV, 1.44 eV, 1.41 eV, 1.36 eV and 1.47 eV. Compared with the original silica tungstic acid forbidden band gap of 3.2 eV, as reported in ref. 27, the band gaps underwent a significant narrowing after modification with Mn–Schiff-base complexes, which was conducive to the improvement of the utilization of light.

3.6 Mott–Schottky analysis

To delve deeper into the influence of different substituents on the light absorption properties of semiconductor materials and investigate their photocatalytic mechanisms, Mott–Schottky analysis was employed. By employing an electrochemical workstation and a standard three-electrode setup to record the Mott–Schottky spectra of compounds **1–5**, their valence and conduction bands were able to be calculated. A positive slope indicates an n-type material, while a negative slope suggests a p-

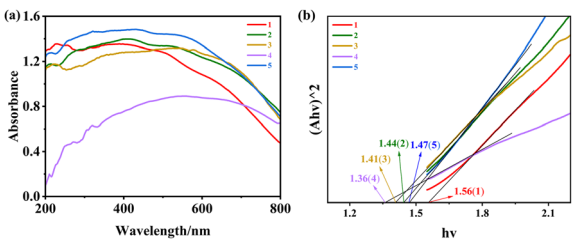

Fig. 4 (a) Solid-state UV/Vis absorption spectra of compounds **1–5**; (b) calculated band gap compounds **1–5**.

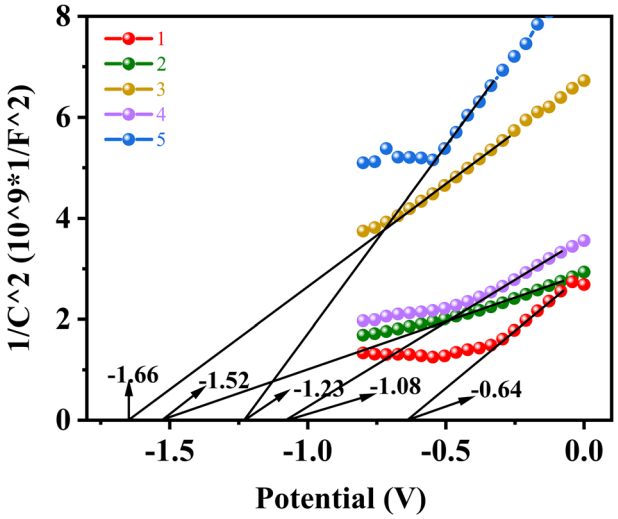

Fig. 5 Flat band potential diagram of compounds **1–5**.

type.[28,29] The results of these tests are presented in Fig. 5. The experimental findings indicate that compounds **1–5** exhibit conventional n-type semiconductor characteristics. The flat band potential of the semiconductor is obtained by making a tangent through the Mott–Schottky analysis.

The flat band potentials of compounds **1–5**, relative to the saturated calomel electrode (SCE), are −0.64 V, −1.52 V, −1.66 V, −1.08 V and −1.23 V. These results suggest that the electron group influences the energy band locations of the semiconductor, favoring negative potentials. Utilizing a saturated calomel electrode (SCE) and the pH of the sodium sulfate solution is equal to 6.80, the conversion of the potential must be transformed by the following equation:

$$E(vs.\ \mathrm{NHE}) = E(vs.\ \mathrm{SCE}) + 0.059 \times \mathrm{pH} + 0.24 \quad (3)$$

The flat band potential corresponds to the Fermi level of the intrinsic semiconductor, while the conduction band potential corresponds to the energy at the bottom of the conduction band. In n-type semiconductors, doping in diverse degrees leads to a corresponding upward shift of the Fermi level, bringing it closer to the bottom of the conduction band. Generally, the conduction band potential for n-type semiconductors is 0.20 V above the flat band potential. It is worth noting that 0.20 is an empirical value and not an exact value.[30,31] By calculating the conduction band potential of the material, the material's energy band positions can be deduced, as detailed in Table 1, in conjunction with solid-state UV diffuse reflection data.

Free radicals ($\cdot OH$, $\cdot O_2^-$, h^+) are thought to be the primary agents in photocatalytic degradation, and the potentials of $\cdot OH$ and $\cdot O_2^-$ relative to the standard hydrogen electrode are known to be around 1.99 eV and −0.33 eV respectively according to the literature.[33] Combining the energy levels and band gap structures of compounds **1–5** above and comparing them with $SiW_{12}O_{40}$, it is found that the band gaps of the energy bands are relatively smaller and the potentials have changed accordingly.

Table 1 Conduction band, valence band, band gap width of compounds **1–5** [a]

Compounds	E_{CB}	E_{VB}	E_g
1	−0.20	1.36	1.56
2	−1.08	0.36	1.44
3	−1.22	0.19	1.41
4	−0.64	0.72	1.36
5	−0.79	0.68	1.47
$SiW_{12}O_{40}$ (ref. 32)	0.05	3.31	3.26

[a] All the electrode potential data in this table are referenced to the saturated calomel electrode (SCE), and its potential is 0.24 V *versus* the standard hydrogen electrode (SHE).

It is postulated that $\cdot O_2^-$ is likely the primary reactive species involved in the process.

3.7 Photocatalytic performance test

The catalyst's catalytic activity was assessed by using RhB. Fig. 6(a) displays a decline in RhB absorption peaks from 2.0 to 0.11 for compound **2**, upon Xe lamp irradiation. Fig. S7(a–d)† displays the outcomes of the experiment, showing a decline in RhB absorption peaks from 2.0 to 0.037, 0.11, 0.398, 0.041, and 0.078 for compound **1** and compounds **3–5**, respectively, upon xenon lamp irradiation. RhB time and relative concentration (C/C_0) are plotted against each other in Fig. 6(b), where the concentration represents the photodegradation of RhB in the presence of artificial sunshine. The findings indicated that among the five catalysts, **2** decayed the fastest, which significantly reduced the catalytic time from 300 minutes to 70 minutes.[8] **1** degraded the most, taking 195 minutes at a 98% degradation rate. Compounds **2** and **3** could achieve almost identical results within 50 min and 150 min, respectively, which could be attributed to their degradation into non-decomposable molecular fragments, with compound **2** having the fastest degradation rate under this reaction condition.[14,34] Notably, compounds **2** and **3**, featuring pull-electronic groups, outperformed compound **1** without electronic groups in photocatalytic efficiency and compounds **4** and **5** with push-electronic groups, which indicates that pull-electronic groups are benefits to enhancing the photodegradation catalyst of POM–Mn–Salen. This observation aligns with our focus on the semiconductor's energy gap and the role of free radical scavenging in investigating the photocatalytic degradation mechanism. As shown in Fig. 7(a), **2** exhibited a more pronounced photocurrent

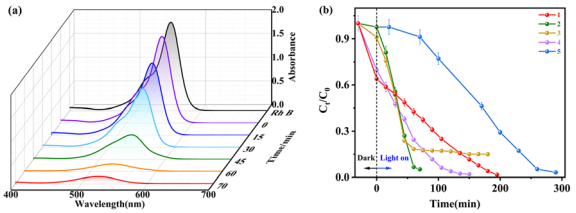

Fig. 6 (a) Photocatalytic degradation of RhB by compound **2** and (b) photocatalytic degradation rate of RhB by compounds **1–5**.

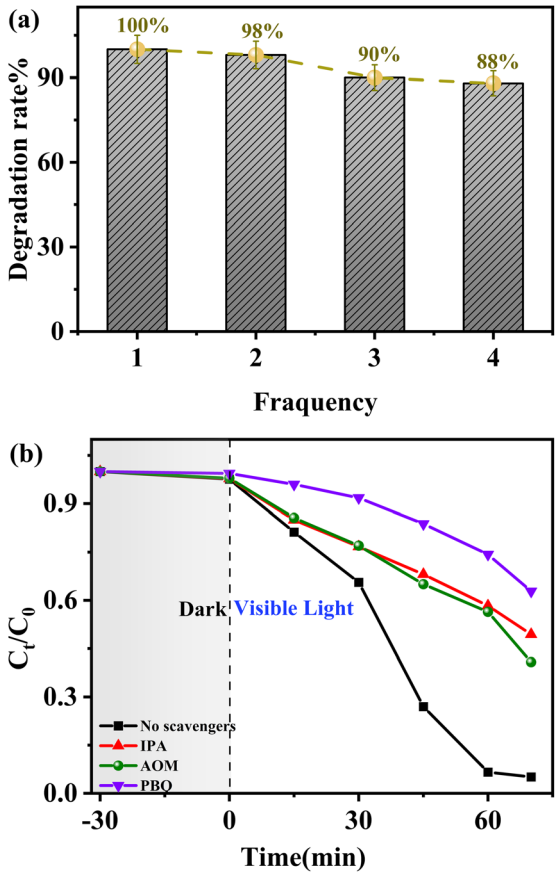

Fig. 7 Recycling of compound 2 within 4 cycles (a) and active species trapping experiments of the compound 2 under visible light irradiation (b).

response, indicating its stronger photogenerated charge separation ability. Meanwhile, 2 has the lowest impedance (Fig. 7(b)), which effectively inhibits photogenerated carrier complexation and thus enhances the catalytic activity. DFT calculations related to organic–inorganic hybrid materials of POMs show that pull-electronic substituents can enable the excited electrons of POMs in the HOMO to transfer more efficiently to the organic complex units in the LUMO.[11–13] This, in turn, can effectively enhance the separation ability of photogenerated electrons and holes and reduce the resistance of electron migration.

3.8 Catalyst stability test

An important investigation of the stability and reusability of catalysts was conducted using four cycles of testing the best catalyzed compound 2. To ensure that the RhB residuals in the pore size of the catalyst surface can be effectively removed, it is necessary to ensure that the experimental conditions in the cyclic experiments are the same as the conditions for photocatalytic degradation. In the meantime, following each cyclic test, the degradation solution was centrifuged in a centrifuge tube, and the supernatant was collected for measurement. The catalyst separated by centrifugation was then repeatedly washed with deionized water and ethanol. As depicted in Fig. 7(a), after four cycles, compound 2 exhibited a negligible degradation activity loss of approximately 12% under visible light, indicating its excellent photostability.

3.9 Free radical trapping experiment

To gain better insights into the photocatalytic mechanism, trapping experiments of reactive species were performed during degradation of RhB by compound 2. Isopropyl alcohol (IPA), oxalic acid (AOM) and *p*-benzoquinone (PBQ) were used as free radicals ·OH, h^+ and $\cdot O_2^-$ trapping agents, in that order. In this experiment, except for the addition of free radical trapping agents into RhB solution, all other conditions were identical to those of photocatalytic degradation, and the experimental results are shown in Fig. 7(b). Under the same circumstances, RhB was degraded within 75 minutes when no free radical inhibitor was added. The RhB degradation rate clearly declines to 37%, 51% and 60% in the presence of PBQ, IPA and AOM, respectively, which demonstrates that the addition of PBQ impacts the photocatalytic activity of the compound 2 the most, followed by IPA and AOM; it also implies that the $\cdot O_2^-$ radicals as major reactive species in the photocatalytic system, plays a major catalytic role in the photocatalytic process[35,36] and can determine the amounts of other active species present, such as ·OH. After adding IPA to trap ·OH, an obvious inhibition of degradation process was observed, indicating that addition of IPA decreased the amount of active ·OH radicals during photocatalytic reactions. The trapped of h^+ by added AOM also inhibited the degradation of RhB. This experimental finding aligns with theoretical predictions regarding the energy band structure.

3.10 Photocatalytic mechanism analysis

Transient photocurrent measurements were employed to look into the photoelectrochemical properties of organic–inorganic hybrid materials. Experiments were conducted using a standard three-electrode setup under a 140 W xenon lamp, and the results are depicted in Fig. 8(a). Compounds 2 and 3 exhibited a more pronounced photocurrent response, which can be observed by alternately switching on and off for five cycles of fifty seconds. It is demonstrated that the two compounds have a greater photocurrent response than the other compounds. This observation indicates that both compounds possess higher

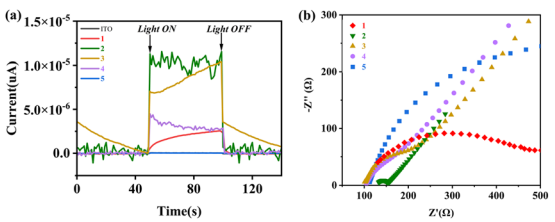

Fig. 8 (a) Transient photocurrent density diagram and (b) electrochemical impedance spectroscopy under a Xe lamp for compounds 1–5.

photogenerated carrier separation and transfer efficiency, as well as enhanced photosensitivity compared to the others.

The radius of curvature in electrochemical impedance spectroscopy (EIS) is inversely associated with the efficiency of photogenerated carrier separation and transfer.[37] The electrochemical impedance spectroscopy (EIS) test, obtained within the 10^5–10^{-2} Hz frequency range and at a test bias voltage of 0 V, is shown in Fig. 8(b). The EIS diagrams of compounds **2** and **3** show smaller arc radii, indicating that they possess faster carrier separation rates. Consistent with the transient photocurrent profile, these findings suggest that incorporating pull-electronic substituted Mn–Schiff-base complexes into semiconductors can effectively suppress photogenerated carrier recombination, thereby boosting the semiconductor's catalytic activity.

When light interaction with the photocatalyst, electrons are excited from the valence band to the conduction band, leaving behind positive holes in the valence band. A hydroxyl radical (·OH) can be produced when the adsorbed water on the surface reacts with the positive holes. Superoxide radical ($\cdot O_2^-$) and hydroxyl radical (·OH) can be produced on the photocatalyst surface when the electrons react with absorbed molecular oxygen.

The energy band analysis above reveals that the conduction band potential of compound **2** is more shifted by −0.33 eV from the potential of $\cdot O_2^-$. And as can be seen from Fig. 7(b), when PBQ is added to the RhB solution, the magnitude of change in the degradation efficiency for the same period of time was only 37%, which suggests that $\cdot O_2^-$ plays an essential role in the degradation of RhB. The potential photocatalytic mechanism for the RhB's degradation by compound **2** photocatalysts was proposed based on the results stated above (Fig. 9). In comparison to $SiW_{12}O_{40}$, compound **2** has a smaller energy band gap, enhancing its sunlight absorption and rapid generation of electron–hole pairs. Under simulated sunlight irradiation, compound **2** is excited to form photogenerated carriers, and the photogenerated electron migration prompts the reduction of O_2 to superoxide radicals ($\cdot O_2^-$), whereas both the generated $\cdot O_2^-$ and holes are capable of oxidative degradation of RhB. Concurrently, h^+ and $\cdot O_2^-$ can react with water to generate hydroxyl radicals (·OH), and ·OH can be reduced with RhB to degrade RhB. As a result, the RhB molecules are degradated by h^+, $\cdot O_2^-$ and ·OH, and these reactions are expressed as follows:

$$\text{Compound } \mathbf{2} + h\nu \rightarrow e^- + h^+ \quad (4)$$

$$e^- + O_2 \rightarrow \cdot O_2^- \quad (5)$$

$$\cdot O_2^- + \text{RhB} \rightarrow \text{degradation products} \quad (6)$$

$$h^+ + \text{RhB} \rightarrow \text{degradation products} \quad (7)$$

$$OH^- + h^+ \rightarrow \cdot OH \quad (8)$$

$$\cdot O_2^- + H_2O \rightarrow \cdot OH \quad (9)$$

$$\cdot OH + \text{RhB} \rightarrow \text{degradation products} \quad (10)$$

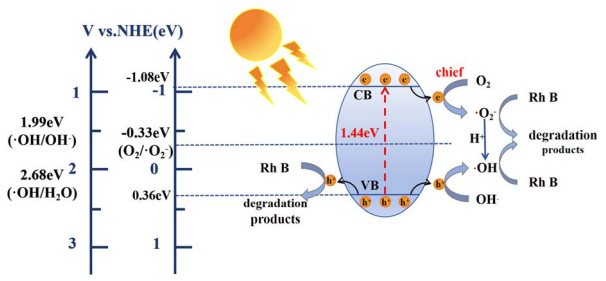

Fig. 9 Schematic diagram of the charge transfer and separation in the compound **2** and possible mechanism of its photocatalytic degradation of RhB under simulated sunlight irradiation.

4 Conclusions

In summary, five Mn–Schiff-base complexes (MnL (L = L^1, L^2, L^3, L^4, L^5)) with distinct substituents were synthesizedto modify $SiW_{12}O_{40}$, resulting in novel compounds **1–5**. The composition of the compounds **1–5** were confirmed through FT-IR, elemental analysis and TGA. Characterization techniques, including UV-Vis DRS, Mott–Schottky, transient photocurrent density, and EIS, revealed that the modified $SiW_{12}O_{40}$ exhibited altered energy band positions and reduced bandgaps, enhancing visible light absorption and carrier separation. For additional research, the compound **2** exhibiting the highest catalytic activity was then subjected to free radical scavenging tests utilizing isopropanol (IPA), oxalic acid (AOM), and para benzoic acid (PBQ) as scavengers. The outcomes were in line with the hypothesis that free radicals were present in the energy band. The potential for $(MnL)_4SiW_{12}O_{40}$ (L = L^1, L^2, L^3, L^4, L^5) in hydrogen production is suggested by its band features and physical qualities. Future research could explore doping or heterojunction strategies to enhance catalytic performance and stability, considering the thermal stability of the compounds.

Data availability

The data that support the findings of this study are available on request from the corresponding author, [Yongfeng Qiao], upon reasonable request.

Author contributions

Yongfeng Qiao: writing – review & editing, conceptualization, methodology, project administration, resources, supervision, data curation, formal analysis; Qiong Wu: writing – review & editing, conceptualization, supervision, data curation; Chang Man: writing – original draft, investigation, data curation, formal analysis, methodology, project administration, funding acquisition; Chunpeng Xu: investigation, data curation, formal analysis, methodology, project administration, funding acquisition; Jinfeng Wang: investigation, data curation, formal analysis, Xiangli Li: methodology, visualization, investigation;

Tong Li: data curation, formal analysis; Yanhua Ma: methodology, formal analysis; Shalu zhang: conceptualization, investigation. All authors discussed the results and reviewed the manuscript.

Conflicts of interest

There are no conflicts to declare.

Acknowledgements

This study acknowledges support from the National Natural Science Foundation of China (No. 21761017). This study is also grateful for the support of the "Yunnan Provincial Department of Education Science Research Fund project (No. 2023Y0902, No. 2024Y752 and No. 2024Y758)".

Notes and references

1 L. Wang, D. W. Bahnemann, L. Bian, G. Dong, J. Zhao and C. Wang, *Angew. Chem.*, 2019, **131**(24), 8187–8192.
2 X. Liu, P. Wang, H. Zhai, Q. Zhang, B. Huang, Z. Wang, Y. Liu, Y. Dai, X. Qin and X. Zhang, *Appl. Catal., B*, 2018, **232**, 521–530.
3 R. Woods-Robinson, Y. Han, H. Zhang, T. Ablekim, I. Khan, K. A. Persson and A. Zakutayev, *Chem. Rev.*, 2020, **120**(9), 4007–4055.
4 M. S. S. Danish, L. L. Estrella, I. M. A. Alemaida, A. Lisin, N. Moiseev, M. Ahmadi, M. Nazari, M. Wali, H. Zaheb and T. Senjyu, *Metals*, 2021, **11**(1), 80.
5 R. Dehghani, S. Aber and F. Mahdizadeh, *Clean:Soil, Air, Water*, 2018, **46**(12), 1800413.
6 L. Yang, M. Xu, H. Wang, D. Zhang and Z. Zhou, *ChemCatChem*, 2024, **16**(14), e202400006.
7 S. Anandan and M. Yoon, *Sol. Energy Mater. Sol. Cells*, 2007, **91**(2–3), 143–147.
8 Q. Wu, W. Chen, D. Liu, C. Liang, Y. Li, S. Lin and E. Wang, *Dalton Trans.*, 2011, **40**(1), 56–61.
9 Q. Wu, S. Lin, Y. Li and E. Wang, *Inorg. Chim. Acta*, 2012, **382**, 139–145.
10 X. Meng, H. Wang, X. Wang, G. Yang, S. Wang, K. Shao and Z. Su, *Inorg. Chim. Acta*, 2012, **390**, 135–142.
11 H. Wu, T. Zhang, L. Yan and Z. Su, *RSC Adv.*, 2015, **5**(113), 93659–93665.
12 T. Zhang, W. Guan, Y. Wei, T. Ma, L. Yan and Z. Su, *Mol. Simul.*, 2016, **42**(8), 688–692.
13 H. Wu, T. Ma, C. Wu, Li. Yan and Z. Su, *Dyes Pigm.*, 2017, **142**, 379–386.
14 X. Meng, H. N. Wang, X. L. Wang, G. S. Yang, S. Wang, K. Z. Shao and Z. M. Su, *Inorg. Chim. Acta*, 2012, **390**, 135–142.
15 X. Meng, C. Qin, X. Wang, Z. Su, B. Li and Q. Yang, *Dalton Trans.*, 2011, **40**(39), 9964–9966.
16 B. M. Pirzada, R. K. Kunchala and B. S. Naidu, *ACS Omega*, 2019, **4**(2), 2618–2629.
17 M. Tang, Y. Ao, C. Wang and P. Wang, *Appl. Catal., B*, 2020, **268**, 118395.
18 X. Sun, J. Zhang and Z. Fu, *ACS Appl. Mater. Interfaces*, 2018, **10**(42), 35671–35675.
19 W. Mäntele and E. Deniz, *Spectrochim. Acta, Part A*, 2017, **173**, 965–968.
20 F. Liu, Y. Li, K. Huang and Z. Xiao, *J. Cent. South Univ. Technol.*, 2007, **14**, 793–797.
21 M. Reagan, E. T. Drew, Z. J. Zhang, C. W. Padgett, J. Orvis and A. Saha, *Inorg. Chem. Commun.*, 2018, **97**, 139–143.
22 K. Kim and J. I. Han, *Int. J. Hydrogen Energy*, 2015, **40**(7), 2979–2983.
23 G.-G. Ying, S. Guo, L. Chen, J. Chen, Y. Li, H. Wang and Y. Liu, *Int. J. Hydrogen Energy*, 2020, **45**(24), 13202–13210.
24 W. A. Shah, A. Waseem, M. A. Nadeem and P. Kögerler, *Appl. Catal., A*, 2018, **567**, 132–138.
25 W. Chen, B. Chen, H. Tan, Y. Li, Y. Wang and E. Wang, *J. Solid State Chem.*, 2010, **183**(2), 310–321.
26 J. Ding, T. Li, X. Wang, M. Li, T. Li and Z. Zhang, *Polymers*, 2024, **16**(16), 2328.
27 G. Yan, X. Feng, L. Xiao, W. Xi, H. Tan, H. Shi, Y. Wang and Y. Li, *Dalton Trans.*, 2017, **46**(46), 16019–16024.
28 Y. Liu, Y. Xu, D. Zhong and N. Zhong, *Chem. Phys.*, 2021, **542**, 111053.
29 S. Hu, B. Chi, J. Pu and L. Jian, *J. Mater. Chem. A*, 2014, **2**(45), 19260–19267.
30 S. Sankaranarayanan, M. Hariram, S. Vivekanandhan and C. Ngamcharussrivichai, *Green Functionalized Nanomaterials for Environmental Applications*, Elsevier, 2022, pp. 417–460.
31 X. Chen, P. Huang, X. Zhu, S. Zhuang, H. Zhu, J. Fu, A. S. Nissimagoudar, W. Li, X. Zhang, L. Zhou, Y. Wang, Z. Lv, Y. Zhou and S. Han, *Nanoscale Horiz.*, 2019, **4**(3), 697–704.
32 G. Yan, X. Feng, L. Xiao, W. Xi, H. Tan, H. Shi, Y. Wang and Y. Li, *Dalton Trans.*, 2017, **46**(46), 16019–16024.
33 W. Yang, X. Du, W. Liu, A. W. Tricker, H. Dai and Y. Deng, *Energy Fuels*, 2019, **33**(7), 6483–6490.
34 H. Yu, B. Wei, J. Wang, H. Zhao, S. Zeng, C. Xue, J. Zhu, Y. Zhang and P. Xu, *New J. Chem.*, 2021, **45**(22), 10063–10069.
35 X. Zhou, X. Liu, X. Huang and H. Ji, *J. Hazard. Mater.*, 2022, **422**, 126869.
36 L. Bai, Y. Cao, X. Pan, Y. Shu, G. Dong, M. Zhao, Z. Zhang, Y. Wu and B. Wang, *Surf. Interfaces*, 2023, **36**, 102612.
37 R. Wei, P. Kuang, H. Cheng, Y. Chen, J. Long, M. Zhang and Z. Liu, *ACS Sustain. Chem. Eng.*, 2017, **5**(5), 4249–4257.